

Optimizing optical properties of bilayer PtSe₂: the role of twist angle and hydrostatic pressure

P. Jureczko,¹ Z. Dendzik,¹ and M. Kurpas¹

Institute of Physics, University of Silesia in Katowice, 41-500 Chorzów, Poland

(*Electronic mail: marcin.kurpas@us.edu.pl)

(Dated: 17 June 2025)

Two-dimensional van der Waals materials offer exceptional tunability in their electronic properties. In this paper, we explore how twisting and hydrostatic pressure can be leveraged to engineer the electronic and optical characteristics of bilayer PtSe₂. Using state-of-the-art first-principles density functional methods, we calculate the electronic band structure and the imaginary part of the dielectric function across multiple twist angles and pressure values. We find, that at the twist angle $\theta = 13.17^\circ$, bilayer PtSe₂, which is intrinsically an indirect semiconductor, transforms into a direct-gap semiconductor. Moreover, we demonstrate that hydrostatic out-of-plane pressure boosts near-infrared optical activity, further expanding the functional potential of PtSe₂ bilayers. The demonstrated high tunability of electronic and optical properties by twisting and pressure opens new application directions of PtSe₂ in optoelectronics.

I. INTRODUCTION

Two-dimensional (2D) transition metal dichalcogenides (TMDC) constitute a big family of materials intensively explored over the recent years. These, so called, *post-graphene* materials display plethora of properties which make them attractive for developing new paradigms of quantum technologies, while the strong structural stability and compatibility with the available fabrication methods^{1,2} make them suitable for industrial and commercial usage. Particularly interesting in this context are semiconductor TMDCs, whose sizable intrinsic band gap allows for broad opto-electronic applications³⁻⁷. Additionally, spin-valley locking in non-centrosymmetric semiconductor TMDCs, enabled by a large spin-orbit coupling in valence bands⁸ allows for optical valley control and selective spin population, creating great conditions for optospintronics and valleytronics applications⁹⁻¹⁴.

Monolayer PtSe₂ is TMDC characterized by robust environmental stability and high room temperature carrier mobility¹⁵⁻¹⁸. Like its bulk counterpart, monolayer PtSe₂ crystallizes in the centrosymmetric octahedral 1T phase. The 1T phase often coexists with the trigonal prismatic 1H phase, which is a metastable state of higher energy, and under light irradiation, it evolves to the 1T phase¹⁹. In the bulk, PtSe₂ is a semimetal with a small overlap of the valence and conduction bands²⁰. In the monolayer limit, it is a semiconductor with a sizable indirect band gap enclosed in a range of 1.2-2 eV.^{21,22}

Owing to the wide energy range of photon transitions, from ultraviolet to mid-infrared²³⁻²⁵, PtSe₂ is a promising material for building optoelectronic devices, such as sensors⁵, photodetectors^{7,17} or photodiodes²⁶. Due to large refracting index it exhibits good lensing properties useful for building ultra-thin flat lenses achieving diffraction-limited focusing and imaging²⁷. The spectrum of applicability in electronic and optoelectronic devices can be further extended by applying strain²⁸⁻³¹ or by exploiting the thickness dependence of the electronic and optical properties^{22,32-35}, which gives additional control over the device parameters. Additionally, in multilayered samples, stacking acts as an extra knob for tailoring materials properties, for instance, photon transition

rates³⁶. However, the significant momentum mismatch between the valence and conduction band edges precludes PtSe₂ from applications as efficient light emitting devices.

Very recently, another method of tailoring materials properties by twisting³⁷ has become a powerful approach for tuning the properties of two-dimensional materials. At its core, it leverages quantum interactions between atoms in stacked layers, which change when the layers are rotated relative to one another. This rotation generates a Moiré pattern, profoundly influencing the material's electronic characteristics. Several fascinating phenomena have been demonstrated to arise due to twist-angle induced correlations, including strongly correlated states³⁷⁻⁴⁰, superconductivity^{41,42}, or electronic decoupling due to large momentum mismatch⁴³. Twist-induced structural changes map also on the optical properties resulting in the observation of long living Moiré excitons⁴⁴⁻⁴⁷ and indirect to direct band gap transitions in semiconductors⁴⁸⁻⁵⁰. In this context, PtSe₂ is very promising material due to PtSe₂ a small energy barrier for the kinetic evolution of interlayer structures, allowing dynamical control of over stackings and twist angles⁵¹.

In this paper, we study the structural, electronic and optical properties of twisted bilayer PtSe₂. Using first-principles calculations, we examine the electronic band structure and optical properties by means of the imaginary part of the dielectric function for five different twist angles ranging from 0° to 60°. We show that by a fine tuning the twist angle θ , the optical activity of bilayer PtSe₂ can be widely controlled. Specifically, for $\theta = 13.17^\circ$, the electronic band gap becomes direct, enabling PtSe₂ as a luminescent material. We also show, that optical activity of PtSe₂ bilayer in the near infrared spectrum can be greatly enhanced by applying hydrostatic pressure. This method has been recently considered as control knob for the spin-orbit proximity effect⁵²⁻⁵⁴ or spin relaxation anisotropy⁵⁵.

Our findings demonstrate that the optical properties of bilayer PtSe₂ can be precisely and extensively tuned using currently available experimental techniques. This paves the way for new applications of PtSe₂, particularly in the development of thin optoelectronic devices, unlocking new possibilities for next-generation technology.

The paper is organized as follows: In the next section, we present the research methodology, including details of the numerical calculations. In Section II, we outline the main results of the paper and discuss their interpretation. Finally, Section III concludes the paper with a summary of the findings.

II. METHODS

First-principles calculations were done using the QUANTUM ESPRESSO open-source DFT package^{56,57}. We used the Optimized Norm-Conserving Vanderbilt SG15 pseudopotentials with the Perdew-Burke-Ernzerhof (PBE) version of the generalized gradient approximation (GGA) exchange-correlation functional^{58,59}. Self-consistency was achieved with the kinetic energy cutoff 50 Ry for the wave function and 200 Ry for charge density. To exclude the interaction between copies of PtSe₂ layers, we introduced a vacuum of 17 Å in the direction perpendicular to the two-dimensional film. Wan der Waals interaction was taken into account using the semiempirical Grimme DFT-D3 dispersion correction. For band gap correction, we used the hybrid Heyd-Scuseria-Ernzerhof (HSE) functional, assuming the typical 20% contribution of the Fock exchange⁶⁰.

Starting from the experimental value $a = 3.7 \text{ \AA}$ ²¹ the lattice constant for monolayer PtSe₂ was optimized using variable cell relaxation based on quasi-Newton scheme implemented in QUANTUM ESPRESSO. We found $a = 3.748 \text{ \AA}$ for monolayer and AA bilayer, while for $\theta = 60^\circ$, the lattice constant adopts $a = 3.727 \text{ \AA}$. Systems with twist angles $\theta = 13.27^\circ$, 21.79° and 32.20° were constructed using the scheme proposed in Ref.⁶¹. Optimized structure parameters are presented in Table I and in Fig. S1 in the Supplemental Material. Self-consistency was achieved with a $21 \times 21 \times 1$ Monkhorst-Pack grid for monolayer, AA and $\theta = 60^\circ$ bilayer. For twist angles $\theta = 13.27^\circ$, 21.79° and 32.20° the k-points mesh was $6 \times 6 \times 1$, $9 \times 9 \times 1$ and $6 \times 6 \times 1$, respectively.

Investigating the optical properties of the materials is possible by analyzing the linear response of the electronic system to an electromagnetic perturbation, such as incoming light. The material response is determined by dielectric function $\epsilon(\omega) = \epsilon_1(\omega) + i\epsilon_2(\omega)$, composed of real $\epsilon_1(\omega)$ and imaginary $\epsilon_2(\omega)$ part. The latter corresponds to the energy absorption of the system and the transition between occupied and unoccupied states. Using Random Phase Approximation, the imaginary complex dielectric tensor $\epsilon_2(\omega)$ can be define in the following form^{62,63}:

$$\text{Im} \epsilon_{ij}(\omega) = \frac{\hbar^2 e^2}{\pi m^2 \omega^2} \sum_{n,n'} \int_{\text{BZ}} \langle n' \mathbf{k} | \hat{p}_i | n \mathbf{k} \rangle \langle n \mathbf{k} | \hat{p}_j | n \mathbf{k} \rangle \left(f_0(\epsilon_{n,\mathbf{k}}) - f_0(\epsilon_{n',\mathbf{k}}) \right) \delta(\epsilon_{n',\mathbf{k}} - \epsilon_{n,\mathbf{k}} - \omega) d\mathbf{k}$$

where n, n' belong to the valence and conduction band, f_0 is a Fermi Dirac distribution, $\hat{p}_{i,j}$ describe the momentum matrix elements between bands n and n' and crystal momentum \mathbf{k} . The real part of the dielectric function can be obtained from the Kramers-Kronig transformation. We consider only

interband transitions occurring between different bands. Such an approach is valid for semiconductors. The dielectric tensor consists of six components related to the system symmetry. For a hexagonal structure, the imaginary dielectric tensor is diagonal with two independent components, $\epsilon_{xx} = \epsilon_{yy} \neq \epsilon_{zz}$. We calculated the imaginary part of the dielectric function for PtSe₂ monolayer and twisted bilayers using the post-processing code *epsilon.x* implemented in QUANTUM ESPRESSO. The mesh convergence for non-self-consistent calculations was achieved with $30 \times 30 \times 1$ k-points for monolayer, $\theta = 0^\circ$ and 60° bilayers. For angles 13.27° , 21.79° and 32.20° the mesh was $9 \times 9 \times 1$, $30 \times 30 \times 1$ and $15 \times 15 \times 1$. We use the broadening parameter *intersmear* for the interband contribution with a value of 0.1 eV in optical transition calculations.

III. RESULTS AND DISCUSSION

A. Electronic structure

We begin with discussing the electronic properties of monolayer PtSe₂ which constitutes the benchmark material for bilayer systems. In Fig. 10 b) we show the calculated band structure of monolayer PtSe₂. As can be seen, single layer PtSe₂ is an indirect gap semiconductor with the gap 1.2 eV obtained for the PBE exchange-correlation potential. Each band is two-fold degenerate owing to inversion symmetric crystal structure of the monolayer. In connection with strong spin-orbit coupling it leads to fast spin relaxation⁶⁴. The lowest two conduction bands (four including spin) form a distinct closed manifold, separated from higher-lying bands by 1.5 eV (not shown). This unique band structure topology fundamentally shapes the low-energy optical spectrum, restricting transitions from the valence band exclusively to these two conduction bands

Let us now discuss bilayer PtSe₂. We prepare bilayer samples by stacking two identical centrosymmetric 1T phase layers one above another and apply a twist of the angle θ . Due to the C_3 rotation axis in a single layer the two limiting twist angles for PtSe₂ bilayers are $\theta = 0^\circ$, and $\theta = 60^\circ$. The former ($\theta = 0^\circ$) corresponds to the AA stacking of the monolayers, see Fig. 10 a). Like in bulk and single layer PtSe₂ the structure of AA stacked bilayer has D_{3d} point group symmetry. The D_{3d} point group contains the inversion operation, which guarantees spin degeneracy of bands at any k-point. Also like the monolayer, the AA bilayer is an indirect gap semiconductor, but with a much smaller band gap 0.2 eV see Fig. 10 e) and Table I. We attribute the gap reduction to the attractive interlayer interaction manifested by a considerable charge accumulation in the interlayer region. This is confirmed by a large peak in the charge density profile $\Delta\rho(z)$, see Fig. S2 a) in the Supplemental Material.

A qualitatively different physics we observe for the twist angle $\theta = 60^\circ$ (AB stacking). In this case, the crystal structure is equivalent to the AA case but with one layer twisted by 180° , see Fig. 10 a), and respects D_{3h} point group symmetry. Now, the bottom Se atom from the upper layer sits on top of another Se atom from the lower layer, which energetically is

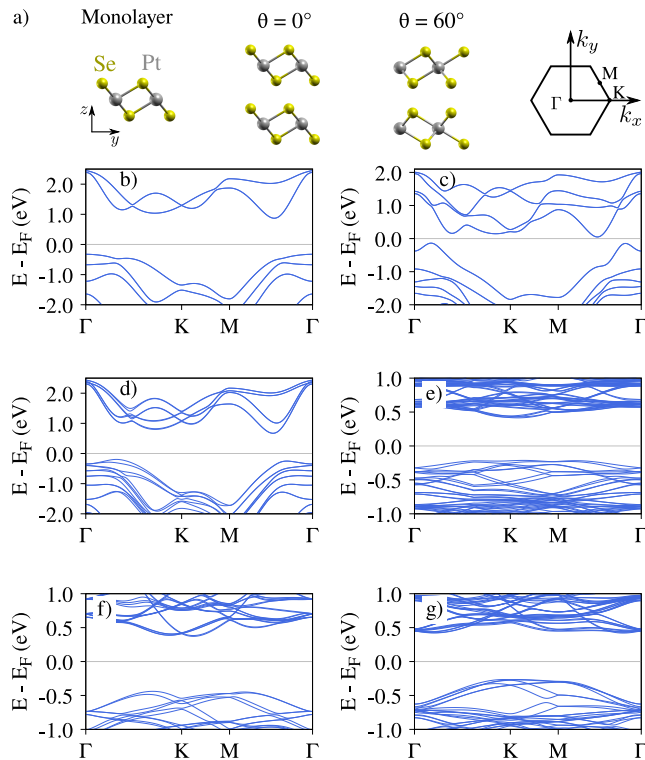


FIG. 1. Electronic properties of mono and bilayer PtSe₂: (a) Sketch of monolayer, 0° and 60° twisted bilayer PtSe₂ crystal structures and the corresponding first Brillouin zone with marked high symmetry points. Calculated relativistic bands structures for single layer (b), and twisted bilayers are shown in (c)-(g) for 0°, 60°, 13.17°, 21.79° and 32.20° respectively.

an unfavorable state and costs an extra 180 meV/atom compared to the AA case. The binding energy for the AB configuration is twice smaller than for the AA case, consistent with other reports³⁶, but is still negative, see Table I, suggesting the structural stability of the AB stacking. Some authors report softening of acoustic modes in phonon spectrum close to the Γ .³⁶ However, it is an artifact attributed to numerical precision rather than to the structural stability issue.^{36,65} Unlike the AA case, now $\Delta\rho(z)$ shows charge depletion in the interlayer region and $\Delta \approx 0$ at $z = 0$, Fig. S2 a) in the Supplemental Material, which indicates a weaker electronic interaction between the layers than for AA case, due to the increased interlayer distance. Such interlayer interaction weakening is linked to low stability local stackings present in twisted systems^{66–69}.

In terms of electronic properties, $\theta = 60^\circ$ case is very similar to monolayer PtSe₂. The band structure remains that of the monolayer PtSe₂, Fig. 10 b) and d) with the number of bands doubled and slightly shifted due to different crystal potentials for the top and bottom layers. Unlike the monolayer, whose Bloch states are spin degenerate due to space inversion symmetry, the states of D_{3h} symmetric AB bilayer are spin split. However, spin degeneracy is maintained along the ΓM direction in the Brillouine zone, which lies on the mirror symmetry plane.

Compared to the monolayer, the bandgap of 60° twisted

TABLE I. Structural and electronic properties of monolayer and twisted bilayer PtSe₂ from first principles.

θ (°)	a (Å)	d _{inter} (Å)	E _g ^{PBE} (eV)	E _g ^{HSE} (eV)
ML	3.748	-	1.2	2.19
0	3.748	2.373	0.2	1.08
60	3.727	3.742	0.85	1.9
13.17	16.34	2.836	0.63	-
21.79	9.92	3.376	0.81	-
32.20	14.67	3.126	0.69	-

bilayer reduces by 0.35 eV to the value 0.85 eV in the case of PBE potential, and by 0.29 eV to the value 1.9 eV for the hybrid HSE pseudopotential, see Table I.

For the intermediate twist angles $\theta = 13.17^\circ$, $\theta = 21.79^\circ$ and $\theta = 32.20^\circ$ the structural properties of PtSe₂ bilayers are similar the each other. They are characterized by similar binding energy, interlayer distance and charge density profile.

The case $\theta = 13.17^\circ$ is the most interesting. In contrast to $\theta = 0^\circ$ and $\theta = 60^\circ$ for this twist angle the band gap is almost direct, see Fig. 10 a). The conduction band edge is only slightly off the valence band edge, by $\delta_k = 0.015 \text{ \AA}^{-1}$, while the energy difference between direct and indirect gap is only 2.3 meV. For such minor discrepancies, the band gap can effectively be treated as direct, highlighting how twisting can transform PtSe₂ into a luminescent material.

It is known that bare exchange correlation potentials systematically underestimate the band gap of semiconductors due to self-interaction errors and missing long-range exact exchange. More accurate approaches, such as GW or hybrid functionals incorporating a fraction of exact Hartree-Fock exchange, yield significantly more realistic band structures but come at a considerably higher computational cost. An extensive analysis of the band structures and optical properties of PtSe₂ systems shows that hybrid functional and GW results can be well reproduced by applying a scissor shift to the conduction bands of PBE results⁷⁰. Thus, we recalculate the band structures using the hybrid HSE potential for configurations with reasonable number of atoms. Our results, shown in Fig. S6 in the Supplemental Material, are in line with Ref.⁷⁰ and indicate that the band structures obtained using the hybrid HSE functional can be well reproduced by the bare PBE functional corrected by a constant scissor shift of conduction bands.

B. Optical properties

Recent experiments supported by theoretical analysis suggest that optical absorption in PtSe₂ in the near-infrared to visible range is dominated by single electron direct transitions, while phonon assisted transitions are negligible⁷⁰. Therefore it is justified to use the single electron approach and describe optical properties by means of the dielectric function $\epsilon(\omega)$:

$\varepsilon(\omega) = \varepsilon_1(\omega) + i\varepsilon_2(\omega)$, composed of real $\varepsilon_1(\omega)$ and imaginary $\varepsilon_2(\omega)$ part. The latter corresponds to the energy absorption due to transitions from occupied to the unoccupied states.

In Fig. 2 we show the calculated imaginary part of dielectric tensor $\varepsilon_{xx/yy}$. For all cases, also for the monolayer, the biggest optical activity is found for photon energies between 1.8 eV - 2 eV. At these energies, transitions from occupied valence states occur exclusively to the lowest conduction band manifold, which is separated from higher-lying bands by approximately 1.5 eV. This energy gap between conduction band manifolds leads to a reduction in the dielectric function within the 3 eV to 5 eV range, as illustrated in Fig. S3 of the Supplemental Material.

For the $\theta = 0^\circ$ bilayer, several peaks appear between 1 eV and 2 eV, resulting from its significantly smaller band gap compared to both the monolayer and the $\theta = 60^\circ$ bilayer. In cases with intermediate twist angles, see Fig. 2 d)-f), the imaginary part of the dielectric function resembles that of the $\theta = 60^\circ$ bilayer but with a slightly broader peak. Overall, the most pronounced effect on the dielectric function is observed for the $\theta = 60^\circ$ bilayer due to its considerably reduced band gap.

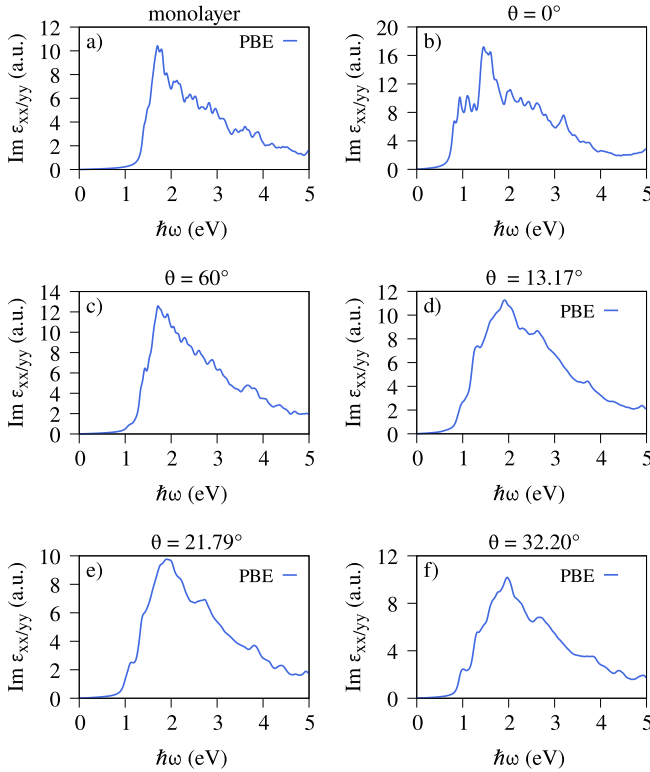


FIG. 2. Imaginary part of dielectric function for monolayer (a), and twisted bilayer PtSe₂ (b)-(g).

To further investigate the origin of the main peak in the dielectric function, we calculated the momentum (dipole) matrix elements between valence and conduction bands within a small energy range of approximately ± 0.7 eV around the peak center at $\hbar\omega \approx 2$ eV. Since spin-orbit interaction has only a minor effect on the overall absorption spectrum (see Figs S3-S6

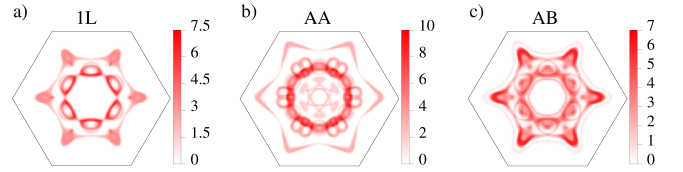


FIG. 3. Momentum matrix elements between valence and conduction bands corresponding to main absorption peak at $\hbar\omega \sim 2$ eV in the energy vicinity ± 0.7 eV around the peak center. Here a non-relativistic approximation is used, see Fig. S3 a)-c).

in the Supplemental Material), we focus on the non-relativistic case and consider the monolayer, $\theta = 0^\circ$, and $\theta = 60^\circ$ bilayers to optimize computational efficiency. The results, shown in Fig. 3, reveal a strong resemblance between the monolayer and $\theta = 60^\circ$ bilayer, reflecting their similar band structures. However, a closer examination uncovers notable differences: for the monolayer (Fig. 3 a)), the highest transition probability occurs at the inner contour, whereas in the AB-stacked bilayer (Fig. 3 c)), the outer contour exhibits a higher transition probability.

In the AA ($\theta = 0^\circ$) case, the most active Brillouin zone region is the hexagon formed around the Γ point, see Fig. 3 b), in particular the points in the ΓK path.

C. Effects of hydrostatic pressure

We now focus on the possibility of tuning the optical properties of PtSe₂ bilayer through the application of hydrostatic pressure. In our first-principles calculations, we simulate hydrostatic pressure in the z (out-of-plane) direction by reducing the bilayer thickness by δd , ensuring that the z coordinates of the outer Se atoms remain fixed at $z \pm \delta d/2$ (see Fig. 4 a)). Next, we allow the structure to relax internal forces and adjust to the in-plane pressure by performing variable cell relaxation while keeping the z coordinates of the outer Se atoms fixed.

The resulting structural parameters, energy gap, and pressure in the z direction are presented in Fig. S1 in the Supplemental Material. As expected, vertical pressure reduces the interlayer distance while inducing a slight expansion of the lattice constant and a flattening of the PtSe₂ layers. Within the experimentally accessible pressure range of 0–3 GPa⁵², controlled stepwise by $\delta d = \{ 0.2 \text{ \AA}, 0.4 \text{ \AA}, 0.6 \text{ \AA}, 0.8 \text{ \AA}, 1 \text{ \AA} \}$, the lattice constant increases by 3% and 1.9%, while the interlayer distance δd decreases by 21% and 17% for the AA and AB stacking configurations, respectively. Additionally, the thickness of the PtSe₂ layer grows with applied pressure, reaching a maximum increase of 6.4% in the AB-stacked bilayer and 9% in the AA-stacked bilayer for $\delta d = 1 \text{ \AA}$.

In Fig. 4 b) and Fig. 4 c), we show the variation of the imaginary part of dielectric function under applied pressure for AA and AB PtSe₂ bilayers, respectively. In both cases, a significant enhancement in optical activity is observed at photon energies between 0.8 eV and 1.5 eV. However, the nature of this enhancement differs between the two stacking configurations. In the AA-stacked bilayer, we observe an increase

in the amplitudes of peaks already present at zero pressure, accompanied by a slight frequency shift toward lower photon energies. By analyzing the dipole matrix elements, we find that this increase in optical activity is directly linked to the energy downshift of the electronic pocket located between the Γ and K points, as shown in Fig. S5 in the Supplemental Material.

In the AB-stacked bilayer, the optical response to applied pressure is significantly stronger than in the AA-stacked case. At zero strain, no active optical transitions occur at $\hbar\omega \sim 1$ eV. However, for $\delta > 0.2$ Å, two electronic pockets, located between the Γ M and Γ K high symmetry points, begin to contribute, with their amplitude increasing as the Fermi contour expands (see Fig. S5 in the Supplemental Material). The overall frequency downshift in the AB-stacked bilayer is approximately 0.75 eV, driven by band gap reduction, and it substantially exceeds the shift observed in the AA-stacked case. The observed effects of hydrostatic pressure on optical properties are similar to those induced by biaxial in-plane strain³⁰. These similarities can be attributed to the stretching of PtSe₂ layers that accompanies the compression of the bilayer.

Due to computational constraints, we did not consider intermediate twist angles in detail. However, an example result obtained for $\theta = 21.79^\circ$ shown in Fig. S7 of the Supplemental Material indicates similar but slightly weaker response of $\epsilon_{xx/yy}$ on the applied strain as for the limiting twist angles $\theta = 0^\circ$ and $\theta = 60^\circ$. For the same reason, we calculated $\epsilon_{xx/yy}$ using hybrid exchange-correlation functionals only for the smallest systems: monolayer, AA and AB bilayers. Results are shown in Fig. S6 in the Supplemental Material. As already mentioned above, in the energy range considered here, the PBE results remain conclusive, taking into account a constant energy shift between PBE and the HSE results.

IV. CONCLUSIONS

We have investigated the electronic and optical properties of monolayer and twisted bilayer PtSe₂. Using first principles calculations we have shown, that for the twist angle 13.17° the electronic band structure of the bilayer transforms into a direct gap semiconductor, opening new perspectives for applications of PtSe₂ as a light emitting devices. Furthermore, we have systematically analyzed the impact of hydrostatic pressure on optical absorption driven in PtSe₂ by direct single electron transitions⁷⁰. Our findings reveal a remarkable tunability of optical properties under pressure, particularly in the near-infrared wavelength range, opening up potential avenues for PtSe₂ in optoelectronics.

ACKNOWLEDGMENT

P. J. and M.K. acknowledge financial support provided by the National Center for Research and Development (NCBR) under the V4-Japan project BGapEng V4-JAPAN/2/46/BGapEng/2022 and support from the Interdisciplinary Centre for Mathematical and Computational Mod-

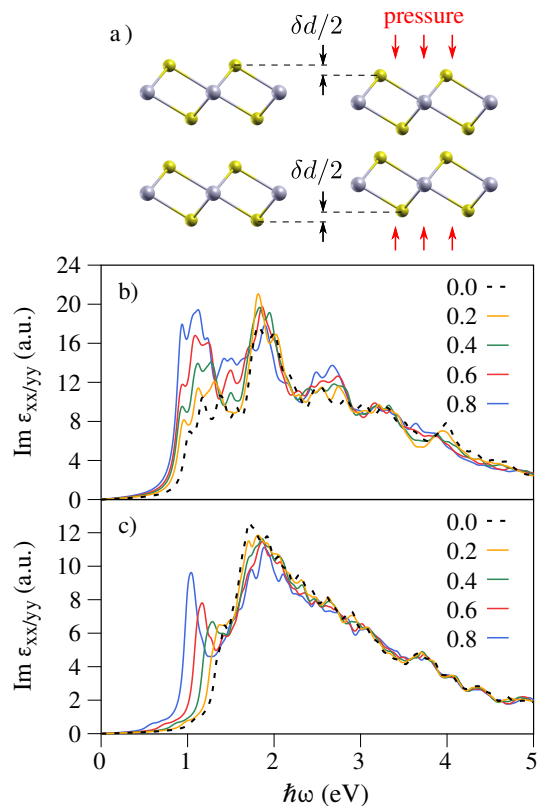


FIG. 4. Bilayer PtSe₂ under hydrostatic pressure: (a) a sketch of simulating hydrostatic pressure in first-principles calculations. Starting from the equilibrium geometry, the outer Se atoms are moved towards the center of the heterostructure. Next, keeping their z -coordinates fixed the structure is relaxed. (b) Imaginary part of the dielectric function versus photon energy for the AA bilayer ($\theta = 0^\circ$) and for various values of structure thickness compression δd given in angstrom. (c) same as (a) but for the AB stacking ($\theta = 60^\circ$).

elling (ICM), University of Warsaw (UW), within grant no. G83-27.

REFERENCES

- S. Meng, Y. Yang, X. Dai, Y. Tang, M. He, Y. Gu, R. Jiang, F. Ding, and H. Xu, *Advanced Functional Materials* **34**, 2312165 (2024), <https://advanced.onlinelibrary.wiley.com/doi/pdf/10.1002/adfm.202312165>.
- H. Xu, H. Zhang, Y. Liu, S. Zhang, Y. Sun, Z. Guo, Y. Sheng, X. Wang, C. Luo, X. Wu, J. Wang, W. Hu, Z. Xu, Q. Sun, P. Zhou, J. Shi, Z. Sun, D. W. Zhang, and W. Bao, *Advanced Functional Materials* **29**, 1805614 (2019), <https://advanced.onlinelibrary.wiley.com/doi/pdf/10.1002/adfm.201805614>.
- M. Koperski, K. Nogajewski, A. Arora, V. Cherkov, P. Mallet, J.-Y. Veuillen, J. Marcus, P. Kossacki, and M. Potemski, *Nature Nanotechnology* **10**, 503 (2015).
- F. Withers, O. D. Pozo-Zamudio, A. Mishchenko, A. P. Rooney, A. Gholinia, K. Watanabe, T. Taniguchi, S. J. Haigh, A. K. Geim, A. I. Tartakovskii, and K. S. Novoselov, *Nature Materials* **14**, 301 (2015).
- S. Wagner, C. Yim, N. McEvoy, S. Kataria, V. Yokaribas, A. Kuc, S. Pindl, C. P. Fritzen, T. Heine, G. S. Duesberg, and M. C. Lemme, *Nano Letters* **18**, 3738 (2018).

- ⁶⁰O. Lopez-Sanchez, D. Lembke, M. Kayci, A. Radenovic, and A. Kis, *Nature Nanotechnology* **8**, 497 (2013).
- ⁷L. Zeng, S. Lin, Z. Lou, and Y. et al., *NPG Asia Materials* **10**, 352 (2018).
- ⁸Z. Y. Zhu, Y. C. Cheng, and U. Schwingenschlöggl, *Phys. Rev. B* **84**, 153402 (2011).
- ⁹K. F. Mak, K. L. McGill, J. Park, and P. L. McEuen, *Science* **344**, 1489 (2014).
- ¹⁰Y. K. Luo, J. Xu, T. Zhu, G. Wu, E. J. McCormick, W. Zhan, M. R. Neupane, and R. K. Kawakami, *Nano Letters* **17**, 3877 (2017).
- ¹¹F. Langer, C. P. Schmid, S. Schlauderer, M. Gmitra, J. Fabian, P. Nagler, C. Schüller, T. Korn, P. G. Hawkins, J. T. Steiner, U. Huttner, S. W. Koch, M. Kira, and R. Huber, *Nature* **557**, 76 (2018).
- ¹²K. Abdukayumov, M. Mičića, F. Ibrahim, L. Vojáček, C. Vergnaud, A. Marty, J. Y. Veuillen, P. Mallet, I. G. de Moraes, D. Dosenovic, S. Gambarelli, V. Maurel, A. Wright, J. Tignon, J. Mangeney, A. Ouerghi, V. Renard, F. Mesple, J. Li, F. Bonell, H. Okuno, M. Chshiev, J. M. George, H. Jaffrès, S. Dhillon, and M. Jamet, *Advanced Materials* **36** (2024), 10.1002/adma.202304243.
- ¹³T. Mueller and E. Malic, *npj 2D Materials and Applications* **2**, 1 (2018).
- ¹⁴R. Dutta, A. Bala, A. Sen, M. R. Spinazze, H. Park, W. Choi, Y. Yoon, and S. Kim, *Advanced Materials* **35**, 1 (2023).
- ¹⁵W. Zhang, Z. Huang, W. Zhang, and Y. Li, *Nano Research* **7**, 1731 (2014).
- ¹⁶Y. Zhao, J. Qiao, Z. Yu, P. Yu, K. Xu, S. P. Lau, W. Zhou, Z. Liu, X. Wang, W. Ji, and Y. Chai, *Advanced Materials* **29** (2017), 10.1002/adma.201604230.
- ¹⁷Y. Yang, S. K. Jang, H. Choi, J. Xu, and S. Lee, *Nanoscale* **11**, 21068 (2019).
- ¹⁸F. Bonell, A. Marty, C. Vergnaud, V. Consonni, H. Okuno, A. Ouerghi, H. Boukari, and M. Jamet, *2D Materials* **9**, 015015 (2021).
- ¹⁹L. Xu, L. Wang, H. Liu, F. Li, D. Li, Y. Cao, C. Wu, X. Bai, and J. Qi, *J. Mater. Chem. C* **9**, 5261 (2021).
- ²⁰G. Y. Guo and W. Y. Liang, *Journal of Physics C: Solid State Physics* **19**, 995 (1986).
- ²¹Y. Wang, L. Li, W. Yao, S. Song, J. T. Sun, J. Pan, X. Ren, C. Li, E. Okunishi, Y.-Q. Wang, and W. et al., *Nano Letters* **15**, 4013 (2015).
- ²²X. Yu, P. Yu, D. Wu, B. Singh, Q. Zeng, H. Lin, W. Zhou, J. Lin, K. Suenaga, Z. Liu, and Q. J. Wang, *Nature Communications* **9**, 1 (2018).
- ²³M. Sajjad, N. Singh, and U. Schwingenschlöggl, *Applied Physics Letters* **112** (2018), 10.1063/1.5010881.
- ²⁴L. P. Slušná, T. Vojteková, J. Hrdá, H. Pálková, P. Siffalovic, M. Sojková, K. Végső, P. Hutár, E. Dobročka, M. Varga, and M. Hulman, *ACS Omega* **6**, 35398 (2021).
- ²⁵S. Bae, S. Nah, D. Lee, M. Sajjad, N. Singh, K. M. Kang, S. Kim, G. J. Kim, J. Kim, H. Baik, K. Lee, and S. Sim, *Small* **17**, 1 (2021).
- ²⁶C. Yim, N. McEvoy, S. Riazimehr, D. S. Schneider, F. Gity, S. Monaghan, P. K. Hurley, M. C. Lemme, and G. S. Duesberg, *Nano Letters* **18**, 1794 (2018).
- ²⁷H. Lin, Z.-Q. Xu, G. Cao, Y. Zhang, J. Zhou, Z. Wang, Z. Wan, Z. Liu, K. P. Loh, C.-W. Qiu, Q. Bao, and B. Jia, *Light: Science & Applications* **9**, 137 (2020).
- ²⁸P. Li, L. Li, and X. C. Zeng, *J. Mater. Chem. C* **4**, 3106 (2016).
- ²⁹P. Li, L. Li, and X. C. Zeng, *Journal of Materials Chemistry C* **4**, 3106 (2016).
- ³⁰S. Deng, L. Li, and Y. Zhang, *ACS Applied Nano Materials* **1**, 1932 (2018).
- ³¹R. Amairi, A. Smiri, and S. Jaziri, *Journal of Physics: Condensed Matter* **37**, 035501 (2024).
- ³²A. Ciarrocchi, A. Avsar, D. Ovchinnikov, and A. Kis, *Nature Communications* **9**, 1 (2018).
- ³³R. A. B. Villaos, C. P. Crisostomo, Z. Q. Huang, S. M. Huang, A. A. B. Padama, M. A. Albao, H. Lin, and F. C. Chuang, *npj 2D Materials and Applications* **3**, 1 (2019).
- ³⁴J. Li, S. Kolekar, M. Ghorbani-Asl, T. Lehnert, J. Biskupek, U. Kaiser, A. V. Krashenninnikov, and M. Batzill, *ACS Nano* **15**, 13249 (2021).
- ³⁵Z. S. Zheng, Z. Peng, Z. S. Yu, H. Lan, S. X. Wang, M. Zhang, L. Li, H. W. Liang, and H. Su, *Results in Physics* **42**, 106012 (2022).
- ³⁶L. Fang, W. Liang, Q. Feng, and S. N. Luo, *Journal of Physics Condensed Matter* **31** (2019), 10.1088/1361-648X/ab34bc.
- ³⁷S. Carr, D. Massatt, S. Fang, P. Cazeaux, M. Luskin, and E. Kaxiras, *Physical Review B* **95**, 1 (2017).
- ³⁸G. Li, A. Luican, J. M. B. Lopes dos Santos, A. H. Castro Neto, A. Reina, J. Kong, and E. Y. Andrei, *Nature Physics* **6**, 109 (2010).
- ³⁹E. Suárez Morell, J. D. Correa, P. Vargas, M. Pacheco, and Z. Barticevic, *Phys. Rev. B* **82**, 121407 (2010).
- ⁴⁰C. R. Dean, L. Wang, P. Maher, C. Forsythe, F. Ghahari, Y. Gao, J. Katoch, M. Ishigami, P. Moon, M. Koshino, T. Taniguchi, K. Watanabe, K. L. Shepard, J. Hone, and P. Kim, *Nature* **497**, 598 (2013).
- ⁴¹Y. Cao, V. Fatemi, S. Fang, K. Watanabe, T. Taniguchi, E. Kaxiras, and P. Jarillo-herrero, *Nature Publishing Group* (2018), 10.1038/nature26160.
- ⁴²L. Klebl, Q. Xu, A. Fischer, L. Xian, M. Claassen, A. Rubio, and D. M. Kennes, *Electronic Structure* **4** (2022), 10.1088/2516-1075/ac49f5.
- ⁴³P. Rickhaus, M.-H. Liu, M. Kurpas, A. Kurzmann, Y. Lee, H. Overweg, M. Eich, R. Pisoni, T. Taniguchi, K. Watanabe, K. Richter, K. Ensslin, and T. Ihn, *Science Advances* **6**, eaay8409 (2020), <https://www.science.org/doi/pdf/10.1126/sciadv.aay8409>.
- ⁴⁴F. Wu, T. Lovorn, and A. H. MacDonald, *Phys. Rev. Lett.* **118**, 147401 (2017).
- ⁴⁵K. Tran, G. Moody, F. Wu, X. Lu, J. Choi, K. Kim, A. Rai, D. A. Sanchez, J. Quan, A. Singh, J. Embley, A. Zepeda, M. Campbell, T. Autry, T. Taniguchi, K. Watanabe, N. Lu, S. K. Banerjee, K. L. Silverman, S. Kim, E. Tutuc, L. Yang, A. H. MacDonald, and X. Li, *Nature* **567**, 71 (2019).
- ⁴⁶F. He, J. Li, L. Li, X. Mao, Z. Liu, S. Teng, J. Wang, and Y. Wang, *Epl* **136** (2021), 10.1209/0295-5075/ac35b9.
- ⁴⁷D. Huang, J. Choi, C.-K. Shih, and X. Li, *Nature Nanotechnology* **17**, 227 (2022).
- ⁴⁸X. G. Gao, X. K. Li, W. Xin, X. D. Chen, Z. B. Liu, and J. G. Tian, *Nanophotonics* **9**, 1717 (2020).
- ⁴⁹K. Xin, X. Wang, K. Grove-Rasmussen, and Z. Wei, *Journal of Semiconductors* **43** (2022), 10.1088/1674-4926/43/1/011001.
- ⁵⁰N. Gupta, S. Sachin, P. Kumari, S. Rani, and S. J. Ray, *RSC Advances* **14**, 2878 (2024).
- ⁵¹L. Xu, H. Liu, C. Song, X. Li, F. Li, D. Li, L. Wang, X. Bai, and J. Qi, *2D Materials* **8** (2021), 10.1088/2053-1583/abd6b6.
- ⁵²B. Fülöp, A. Márffy, S. Zihlmann, M. Gmitra, E. Tóvári, B. Szentpéteri, M. Kedves, K. Watanabe, T. Taniguchi, J. Fabian, C. Schönenberger, P. Makk, and S. Csonka, *npj 2D Materials and Applications* **5**, 1 (2021).
- ⁵³M. Kedves, B. Szentpéteri, A. Márffy, E. Tóvári, N. Papadopoulos, P. K. Rout, K. Watanabe, T. Taniguchi, S. Goswami, S. Csonka, and P. Makk, *Nano Letters* **23**, 9508 (2023).
- ⁵⁴M. Milivojević, M. Kurpas, M. Rassekh, D. Legut, and M. Gmitra, *Phys. Rev. B* **110**, 085306 (2024).
- ⁵⁵P. Jureczko, M. Milivojević, and M. Kurpas, *New Journal of Physics* **27**, 053006 (2025).
- ⁵⁶P. Giannozzi, S. Baroni, N. Bonini, M. Calandra, R. Car, C. Cavazzoni, D. Ceresoli, G. L. Chiarotti, M. Cococcioni, I. Dabo, A. D. Corso, S. de Gironcoli, S. Fabris, G. Fratesi, R. Gebauer, U. Gerstmann, C. Gougoussis, A. Kokalj, M. Lazzeri, L. Martin-Samos, N. Marzari, F. Mauri, M. Mazzarello, S. Paolini, A. Pasquarello, L. Paulatto, C. Sbraccia, S. Scandolo, G. Sclauzero, A. P. Seitsonen, A. Smogunov, P. Umari, and R. M. Wentzcovitch, *Journal of Physics: Condensed Matter* **21**, 395502 (2009).
- ⁵⁷P. Giannozzi, O. Andreussi, T. Brumme, O. Bunau, M. B. Nardelli, M. Calandra, R. Car, C. Cavazzoni, D. Ceresoli, M. Cococcioni, N. Colonna, I. Carnimeo, A. D. Corso, S. de Gironcoli, P. Delugas, R. A. DiStasio, A. Ferretti, A. Floris, G. Fratesi, G. Fugallo, R. Gebauer, U. Gerstmann, F. Giustino, T. Gorni, J. Jia, M. Kawamura, H.-Y. Ko, A. Kokalj, E. Küçükbenli, M. Lazzeri, M. Marsili, M. Marzari, F. Mauri, N. L. Nguyen, H.-V. Nguyen, A. O. de-la Roza, L. Paulatto, S. Poncè, D. Rocca, R. Sabatini, B. Santra, M. Schlipf, A. P. Seitsonen, A. Smogunov, I. Timrov, T. Thonhauser, P. Umari, N. Vast, X. Wu, and S. Baroni, *Journal of Physics: Condensed Matter* **29**, 465901 (2017).
- ⁵⁸D. R. Hamann, *Phys. Rev. B* **88**, 085117 (2013).
- ⁵⁹J. P. Perdew, K. Burke, and M. Ernzerhof, *Phys. Rev. Lett.* **77**, 3865 (1996).
- ⁶⁰J. Heyd, G. E. Scuseria, and M. Ernzerhof, *The Journal of Chemical Physics* **118**, 8207 (2003).
- ⁶¹K. Uchida, S. Furuya, J.-I. Iwata, and A. Oshiyama, *Phys. Rev. B* **90**, 155451 (2014).
- ⁶²C. Ambrosch-Draxl and J. O. Sofo, *Computer Physics Communications* **175**, 1 (2006).
- ⁶³S. L. Adler, *Physical Review* **126**, 413 (1962).

- ⁶⁴M. Kurpas and J. Fabian, *Physical Review B* **103**, 1 (2021).
- ⁶⁵A. Kandemir, B. Akbali, Z. Kahraman, S. V. Badalov, M. Ozcan, F. Iyikanat, and H. Sahin, *Semiconductor Science and Technology* **33** (2018), 10.1088/1361-6641/aacba2.
- ⁶⁶K. Liu, L. Zhang, T. Cao, C. Jin, D. Qiu, Q. Zhou, A. Zettl, P. Yang, S. G. Louie, and F. Wang, *Nature Communications* **5**, 4966 (2014).
- ⁶⁷P. K. Nayak, Y. Horbatenko, S. Ahn, G. Kim, J.-U. Lee, K. Y. Ma, A.-R. Jang, H. Lim, D. Kim, S. Ryu, H. Cheong, N. Park, and H. S. Shin, *ACS Nano* **11**, 4041 (2017), PMID: 28363013.
- ⁶⁸W. Yan, L. Meng, Z. Meng, Y. Weng, L. Kang, and X.-a. Li, *The Journal of Physical Chemistry C* **123**, 30684 (2019).
- ⁶⁹J. Ahn, S.-H. Kang, M. Yoon, and J. T. Krogel, *Phys. Rev. Res.* **6**, 033177 (2024).
- ⁷⁰M. Tharrault, S. Ayari, M. Arfaoui, E. Desgué, R. L. Goff, P. Morfin, J. Palomo, M. Rosticher, S. Jaziri, B. Plaçais, P. Legagneux, F. Carosella, C. Voisin, R. Ferreira, and E. Baudin, *Physical Review Letters* **134**, 066901 (2025).

SUPPLEMENTAL MATERIAL: OPTIMIZING OPTICAL PROPERTIES OF BILAYER PtSe_2 : THE ROLE OF TWIST ANGLE AND HYDROSTATIC PRESSURE

Structural and electronic properties of PtSe_2 bilayers under hydrostatic pressure

In Fig. 5 we show how the structural and electronic properties of AA and AB bilayers change with increasing hydrostatic pressure defined by δd (thickness reduction of the bilayer). We see, Fig. 5 a), that with growing δd the lattice constant expands to relax the generated in-plane stress. The corresponding out-of-plane pressure and the reduction of the interlayer distance d_{inter} are presented in Fig. 5 a) and c), respectively. The relative structural response of AA and AB bilayers to the applied pressure is similar, however, a slightly bigger pressure values for AA than for AB case are observed, most probably due to the much smaller initial interlayer distance.

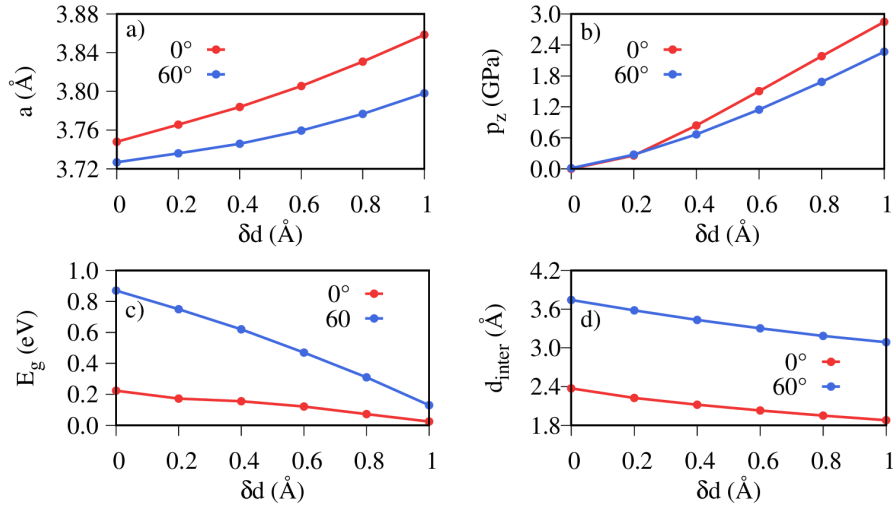


FIG. 5. Parameters of strained 0° and 60° systems; a) cell parameter, b) pressure along z-direction, c) size of the band gap, d) interlayer distance along z-direction (between selenium atoms).

Charge density profile

To get an insight into the details of the interlayer interaction, we calculate the charge density profile $\Delta\rho$ within the simulation cell for each bilayer system. We define $\Delta\rho$ as the difference of charge density of the bilayer minus charge density of two non-interacting monolayers placed at the same positions as in the bilayer:

$$\Delta\rho(z) = \int_S (\rho_{BL} - [\rho_U + \rho_L]) dxy, \quad (1)$$

where ρ_{BL} is the charge density of the bilayer, and ρ_U and ρ_L are charge densities of the upper and lower monolayer, respectively, and S is the area of the unit cell in the xy plane. Qualitative differences between the AA ($\theta = 0^\circ$), and twisted bilayers are evident, see Fig. 6.

For comparison, the band structure of single-layer PtSe_2 is shown in Fig. 10 a).

Comparison of non-relativistic and relativistic calculations

In heavy element materials, spin-orbit coupling considerably modifies the band structure, opening spin-orbital gaps of hundreds meV. In PtSe_2 SOC opens orbital gaps from tens meV up to 300 meV at the Γ point in the valence band⁶⁴, thus it cannot be neglected.

In Fig. 7 we show the calculated imaginary part of the dielectric function. A direct comparison with Fig. 2 in the main text indicates, that $\text{Im}\epsilon_{xx/yy}$ for relativistic case displays slightly smoother shape than for non-relativistic one due lifted band degeneracy, while the overall shape of $\text{Im}\epsilon_{xx/yy}$ remains the same.

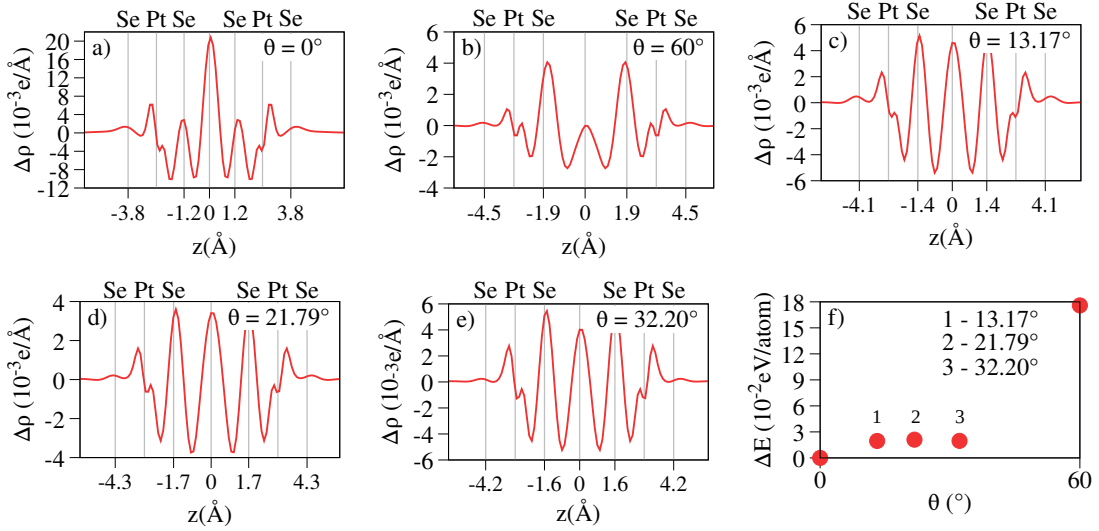


FIG. 6. Charge density difference profile of the a) 0° , b) 60° , c) 13.17° , d) 21.79° , e) 32.20° and f) comparison of total energy difference for all systems, with regard to AA.

This is confirmed by looking at momentum matrix elements calculated using non-relativistic and relativistic approximations shown in Fig. 8. As can be seen, the inclusion of SOC does not lead to qualitatively different results. Thus, the non-relativistic approximation is valid for explaining essential features of optical transitions.

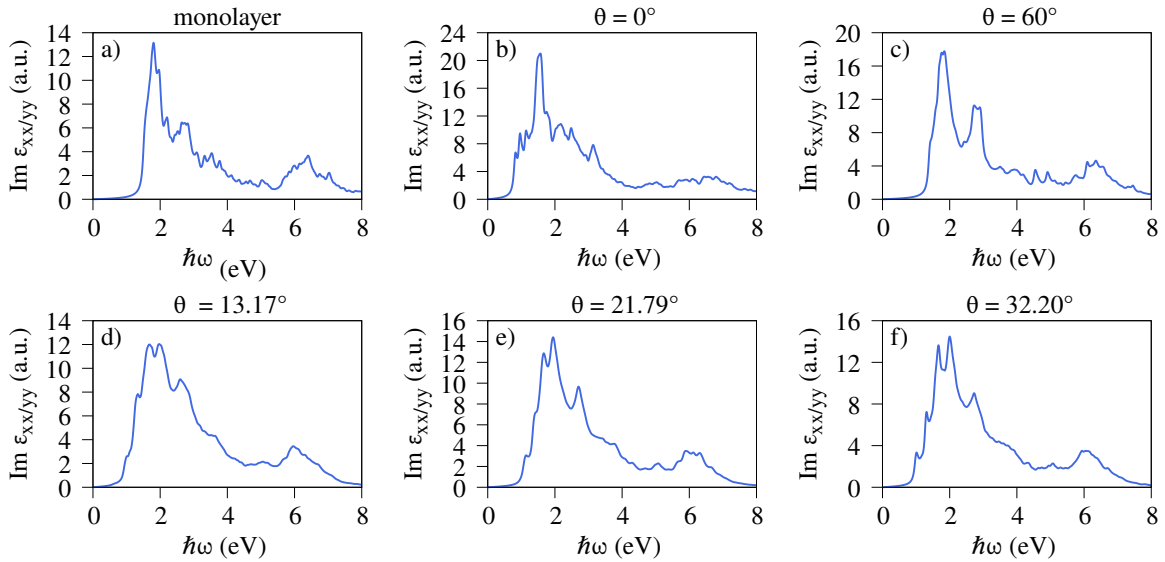


FIG. 7. Imaginary part of dielectric tensor for a) monolayer, b) 0° , c) 60° , d) 13.17° , e) 21.79° and f) 32.20° calculated without spin-orbit coupling interaction.

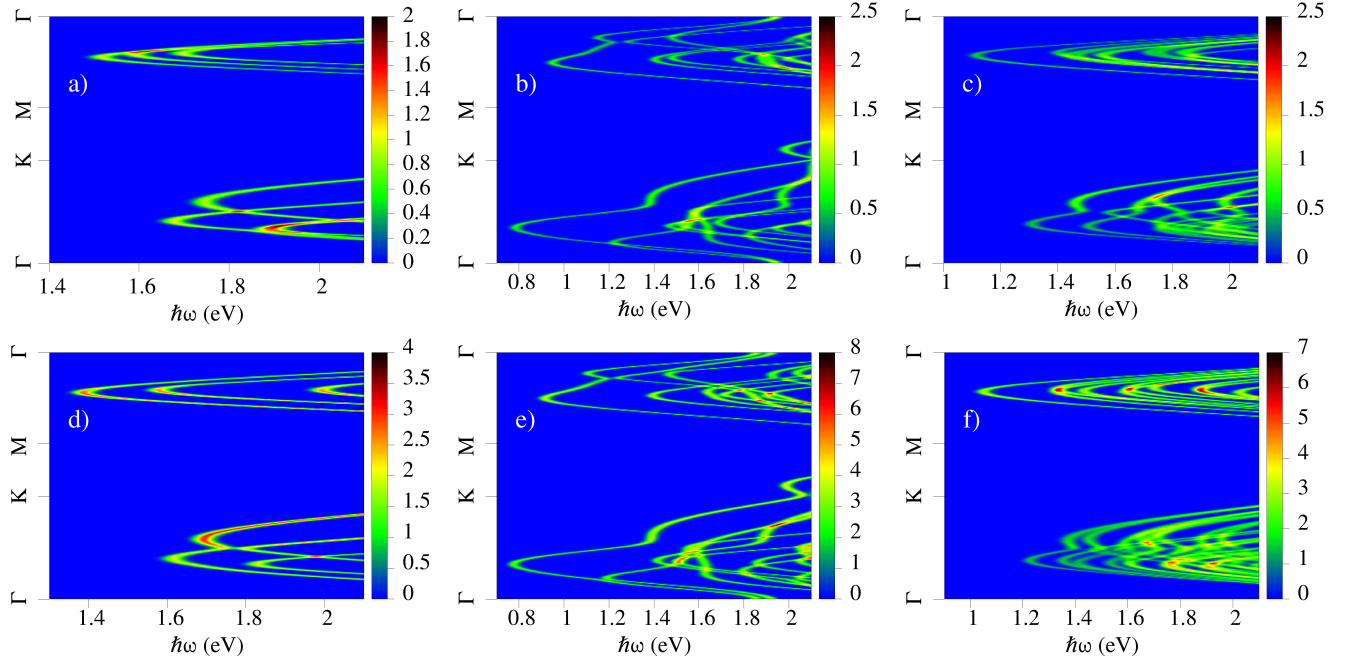


FIG. 8. Comparison of momentum matrix elements calculated without (top row) and with spin-orbit coupling (bottom row) for the monolayer (left column), AA bilayer (middle column) and AB bilayer PtSe₂ (right column). For relativistic calculation in monolayer and AA case an infinitesimal (10^{-6} V/nm) transverse electric field was applied to remove the bands degeneracy and the arbitrariness of choice of eigenvectors.

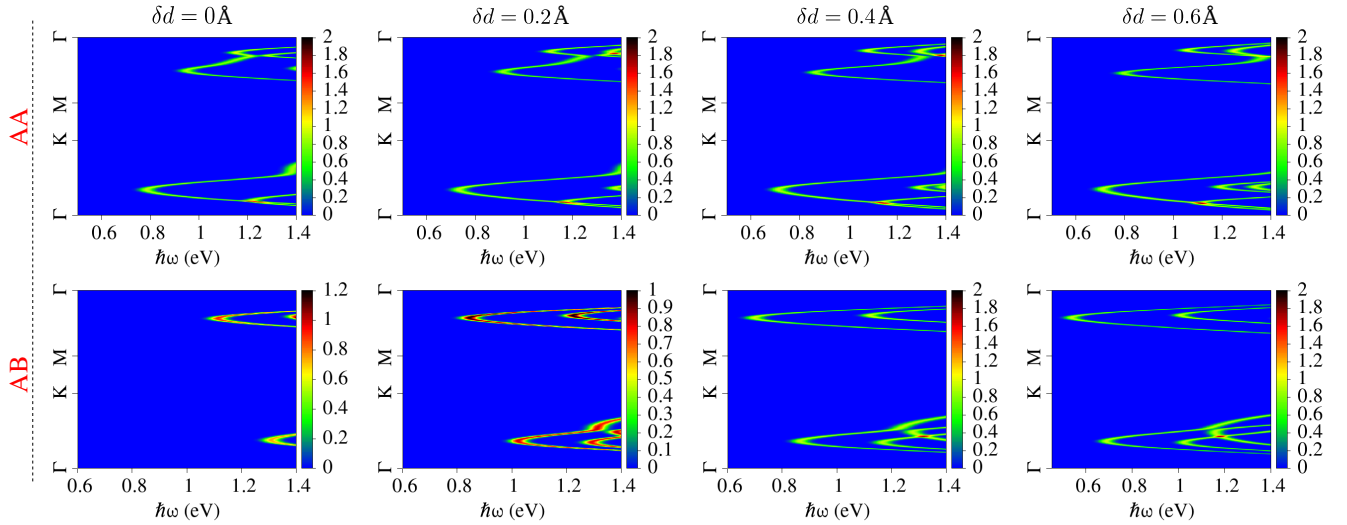


FIG. 9. Momentum matrix elements for the AA (top row) and AB (bottom row) calculated for k-points along high symmetry lines of the first Brillouin zone versus photon energy $\hbar\omega$ and for several values of hydrostatic pressure. Calculation without spin-orbit coupling.

Comparison of PBE and hybrid exchange-correlation functionals

We have performed first principles calculations using the hybrid Heyd-Scuseria-Ernzerhof (HSE) functional, assuming 20% contribution of the Fock exchange⁶⁰. The calculated band structures shown in Fig. 10 a) - c) show minor discrepancies between PBE and HSE functionals, except a constant energy offset of the conduction bands. Similar conclusions were drawn in Ref.⁷⁰.

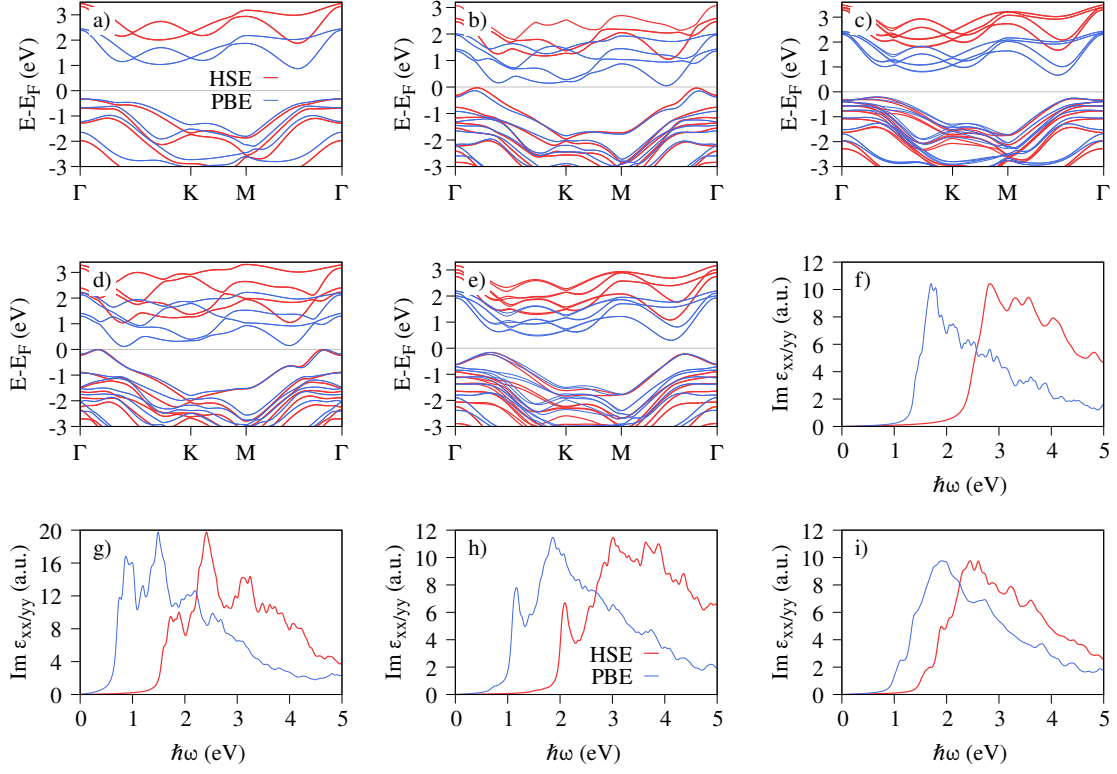


FIG. 10. Comparison of PBE and hybrid HSE calculations. Relativistic band structures of the monolayer (a), AA bilayer ($\theta = 0^\circ$) (b) and AB bilayer ($\theta = 60^\circ$) PtSe₂. (d),(e) - band structures for AA and AB stackings with applied hydrostatic pressure $\delta d = 0.6 \text{ \AA}$. The corresponding plots of the imaginary part of dielectric function are shown in (g) and (h), respectively. (f),(i) - imaginary part of the dielectric tensor for the monolayer and $\theta = 21.79^\circ$ twisted bilayer PtSe₂.

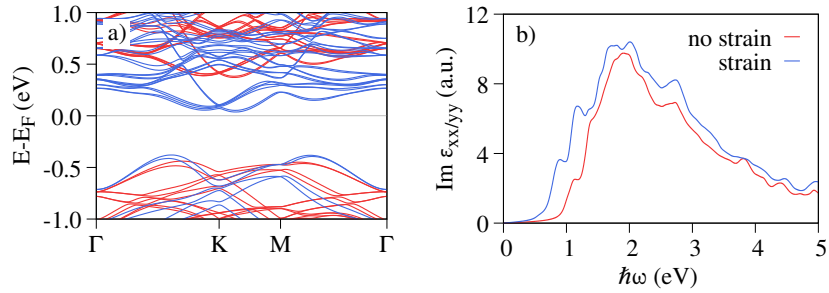


FIG. 11. Relativistic band structures (a) and dielectric function (b) for $\theta = 21.79^\circ$ - twist angle for unstrained (red line) and under hydrostatic pressure $\delta d = 0.6 \text{ \AA}$ bilayer PtSe₂.